Modelling capacity fade in silicon-graphite composite **electrodes** for lithium-ion batteries

Shweta Dhillon [a],*, Guiomar Hernández [a], Nils P. Wagner [b,c], Ann Mari Svensson [b], Daniel Brandell [a]

[a] Department of Chemistry - Ångström Laboratory, Uppsala University, Box 538, SE-751 21, Uppsala, Sweden
[b] Department of Material Science and Engineering, Norwegian University of Science and Technology (NTNU), Høgskoleringen 1, NO-7491, Trondheim, Norway
[c] Department of Sustainable Energy Technology, SINTEF Industry P.O.Box 4760 Torgarden, NO-7465 Trondheim, Norway

A R T I C L E   I N F O

A B S T R A C T

Silicon-based composite electrodes in lithium ion batteries attract increasing attention because of their high theoretical capacity. Here, numerical simulations are used to better understand the interplay between electrochemical and morphological behavior of the silicon-graphite (1:2.7) composite electrode during galvanostatic cycling. Finite element methodology is used to solve a one-dimensional model based on the porous electrode and concentrated solution theory. Porosity changes in the silicon electrode and solid electrolyte interphase layer growth are also included in the model. The simulation results show that at lower rates, the electrode with high initial porosity is being fully utilized before the lower cut-off potential is reached. When comparing the computational results with experimental observations, it can be seen that the main reason for capacity fade is the increase in tortuosity in the diffusion pathway of lithium ions due to cracking of the silicon composite electrode upon electrochemical cycling.

© 2021 Elsevier Ltd. All rights reserved.

1. Introduction

The increasing demand for electric vehicles, hybrid electric vehicles and plug-in hybrid electric vehicles has spurred interest in using silicon as a component in lithium ion battery anodes. Silicon has a high theoretical specific capacity ($3590 mAh g^{-1}$; corresponding to $Li_{15}Si_4$), almost 10 times higher than the widely used and commercially dominating graphite anodes ($\sim 372\ mAh g^{-1}$) [1,2]. More widespread implementation of silicon-based anodes is, however, held back, due to primarily two major obstacles: volume expansion during lithiation and side reactions occurring at the silicon/electrolyte interface [3,4]. These two phenomena are also interconnected, since the volume expansion exposes more surface of the active material for side reactions to take place at. These continuous side reactions at the silicon/electrolyte interface thereby result in electrolyte decomposition, and the cells then gradually suffers from a loss of active lithium [4,5].

At room temperature, 250-280% volume expansion have been observed in the active silicon material during lithiation [4,6], with a similar contraction during delithiation. These volume changes

during charging/discharging generally occur in two different ways: void volume changes and/or changes in the dimensions of the porous electrode [6]. Silicon active particles expand upon lithiation into the void fraction of the anode. A highly porous anode can accommodate large volume changes without change in the dimensions of the porous electrode. This implies that even though volume changes in individual silicon particles are large, the overall electrode dimension will not be significantly affected. This does not hold true, however, for less porous electrodes where dimensional changes can be substantial. Thus, it is important to account for porosity changes in lithium-silicon systems.

Repeated lithiation/delithiation of silicon particles can cause isolation of active material, which prevents further electrochemical activity, and subsequently lead to capacity losses. Moreover, silicon electrodes which are based on micron sized particles can suffer from particle pulverization upon repeated cycling, which also often results in loss of electronic contact in the electrode. Therefore, the reversible capacity of most silicon anodes decays after a few cycles [7,8]. A promising strategy to mitigate these losses, and which have shown considerable progress recently, has been to design silicon nanostructures that resist fracture or have dimensionally stable surfaces for solid electrolyte interphase (SEI) growth [9,10]. However, a decrease in particle size also leads to inferior electronic conduction and low coulombic efficiency due to a large specific surface area [2,11], and to more costly electrodes. More-

---

* Corresponding author.
E-mail addresses: shweta.dhillon@kemi.uu.se, dhillon_shweta007@yahoo.co.in (S. Dhillon).

over, at room temperature, the Li-Si systems display a range of additional challenges as compared to elevated temperatures. These are associated with slow reaction kinetics [12], slow diffusion processes [12,13] and low electronic conductivity [14]. The silicon volume change will result in electrode active surface area changes that certainly will affect the SEI layer formation and is thus an important factor for the overall cell behavior [15]. Recently, effects of particle pulverization and its correlation with SEI formation and charge transfer resistances were observed electrochemically for silicon/graphite composite electrodes with different carbon/silicon ratio using impedance analysis [16]. The silicon volume change will result in electrode active surface area changes that certainly will affect the SEI layer formation and is thus an surface area change is important factor affecting the overall cell behavior [15]. Recently, the effect of pulverization and its correlation with the SEI and charge transfer resistances was electrochemically observed for silicon/graphite composite electrodes with different carbon/silicon ratio using EIS analysis [16].

Computational modelling of lithium ion batteries has been growing extensively in recent years and is becoming a necessary tool to analyze a vast range of degradation phenomena in these electrochemical cells [17–21]. In such studies, a theoretical analysis of the porosity changes has been shown to be important since the effective transport properties of the electrolyte, such as the diffusion coefficient of the lithium ions in the electrolyte and the ionic conductivity decrease with the decline in porosity [22]. For example, Srivastav et al. have discussed the evolution of electrode morphology and its effect on electrochemical performance during cycling of Si-based battery electrodes. When the void volume gets smaller during lithiation, the ionic current flows through a narrow path in the electrolyte phase occupying the pores, which will lead to a higher ionic resistance [23,24]. Chandrasekaran et al. have in this context reported a theoretical framework which account for the effects of porosity changes on cell performance, including convection effects along with the general description of transport in the electrolyte phase based on concentrated solution theory [20,25].

To overcome the limitations of silicon anodes, silicon composites with other active materials have been explored. In these, graphite is typically used along with silicon because of its high electrical conductivity, dimensional stability and traditional use in lithium ion batteries, allowing for fabrication of electrodes which can accommodate the volume changes of the silicon [26–29], provided that the fraction of silicon is kept low. For example, Beattie et al. have shown that a Si-graphite electrode which comprise less than 20 wt% Si can accommodate the large volume expansions [30]. However, a detailed computational model of silicon-graphite composite anodes is still largely missing. Thereby, it is still poorly understood how changes in the porous structure, both during lithiation and over repeated cycling, affect its cycling performance and capacity retention. Therefore, we have here developed a model that links electrochemical and morphological phenomena in these composite anodes.

In this study, we present an extensive concentration solution theory approach to understand capacity fade in silicon-graphite composite electrodes in a half-cell model. The model is developed within the framework of the porous electrode theory. We have also included the impact of SEI film formation in the composite anode, which is a decisive ageing phenomenon. The model provides a predictive tool for the cycling performance of silicon-graphite composite anodes and has been employed to study the evolution of electrode morphology during cycling, caused by the continuous expansion and contraction of silicon particles. The model is benchmarked against experimental data and used to better understand the structural changes and its effect on electrochemical performance. In addition, the most reasonable degradation mechanism in terms of

microcracks is identified based on comparison to simulation results and incorporated into the model description.

2. Experimental

2.1. Materials

LP57 electrolyte (BASF, 1 M LiPF$_6$ in ethylene carbonate:ethyl methyl carbonate (EC:EMC) 3:7 v/v), fluoroethylene carbonate (FEC, Gotion, battery grade) and vinylene carbonate (VC, Gotion, battery grade) were used as received. Lithium 4,5-dicyano-2-(trifluoromethyl)imidazole (LiTDI) was provided by the Polymer Ionics Research Group at Warsaw University of Technology; the synthesis has been reported elsewhere [31]. LiTDI was dried at 120°C for 12 h under vacuum. The electrolyte was prepared by adding 10 wt% FEC, 2 wt% VC and 2 wt% LiTDI to the LP57 electrolyte.

2.2. Electrode preparation

Silicon-graphite composite electrodes were prepared from 22 wt% silicon (Silgrain e-Si 400, ELKEM), 60 wt% graphite (TIMREX SLP30, Imerys), 10 wt% conductive carbon black (TIMCAL C-NERGY^{TM} Super C 65, Imerys), 5.5 wt% carboxymethyl cellulose as binder (CMC) and 2.5 wt% of buffer chemicals (citric acid/potassium citrate pH 3). The average radius of the silicon particle was 1.7 μm while graphite was 8 μm. Circular electrodes ($\phi = 13$ mm) were punched out and further dried at 120°C under vacuum for 12 h prior to battery assembly. The active areal mass loading of silicon-graphite composite was ~ 4.6 mg cm^{-2}. All batteries were assembled as pouch cells in an argon glovebox (O$_2$, H$_2$O < 5 ppm). Two-electrode half cells were assembled using lithium metal ($\phi = 15$ mm) as counter and reference electrode and one piece of Celgard 2325 separator ($\phi = 17$ mm) which was soaked with 50 μL of electrolyte unless otherwise stated.

2.3. Electrochemical characterizations

Galvanostatic cycling of these cells was performed on an Arbin BT 2043 battery tester. A pre-cycling step was applied at a constant current of C/20 (based on a reversible capacity of 1015 $mAh\,g^{-1}$ of the silicon-graphite composite electrode) between 0.05 and 1.50 V with a constant voltage step after lithiation until the current dropped to C/50. Long-term cycling was carried out at C/2 between 0.05 and 1.50 V with a constant voltage step after lithiation and delithiation with a limiting capacity of 800 $mAh\,g^{-1}$ (78.8 % state of charge, SOC) or when the current dropped to C/125.

3. Model description

The model system considered in this work is a cell comprising silicon-graphite composite electrode/separator/lithium foil. The half-cell lithium battery model consists of the cell cross section in one dimension, implying that edge effects in length and height are neglected. The cell has the following geometry:

1. x = 0 : Negative current collector boundary.
2. 0<x< δ_n : Porous silicon-graphite composite electrode. Thickness: 45 μm.
3. δ_n <x< δ_s Separator (1M LiPF$_6$ in EC:EMC in a 3:7 ratio with 10 wt% FEC, 2 vol% of VC and 2 wt% of LiTDI. Thickness: 25 μm.
4. δ_s <x< δ_p: Counter electrode (lithium foil). Thickness: 20 μm.

For the electronic current balance, the counter electrode boundary is grounded, i.e. $V = 0$ ($x = \delta_p$), and charging and discharging conditions is applied at the interface between the working electrode and the current collector ($x = 0$). The inner boundaries, at

Table 1
Table of symbols.

Symbol	Description
a	particle specific interfacial area, $1/m$
c	concentration of the electrolyte, mol/m^3
c_s	concentration of lithium in the solid particle phase, mol/m^3
c_{max}	maximum lithium concentration in solid phase, mol/m^3
D_{Li^+}	bulk diffusion coefficient of the lithium salt, m^2/s
D_{eff}	effective diffusion coefficient of the lithium salt, m^2/s
F	Faraday's constant, 96487 C/eq
i	current density, A/m^2
i_2	solution (electrolyte) phase current density, A/m^2
i_n	transfer current per unit of interfacial area, A/m^2
i_0	exchange current density for lithium insertion in silicon composite electrode, A/m^2
I_{app}	Applied current density (for C/2 rate) (negative for lithiation and positive for delithiation)
k	reaction rate constant, m/s
m_{sei}	average molecular weight of SEI, g/mol
p	tortousity factor
R_s	radius of solid silicon spherical particles (here taken to be constant), m
R_{sp}	varying radius of solid silicon spherical particles used in the expression for a
s_i	stoichiometric coefficient of species i in electrode reaction
t_+^0	transference number of Li^+ relative to the solvent
t	time, s
T	temperature, K
U	open-circuit potential (as a function of x_s) of silicon composite electrode vs. Li/Li^+ ref., V
$v^{\#}$	superficial volume average velocity, m/s
$\tilde{V}_{LiSi_{4/15}}$	molar volume of $Li_xSi_{4/15}$ in the electrode, m^3/mol
$\overline{V}_{Si}$	partial molar volume of $Si_{4/15}$ in the electrode, $12 \times 10^{-6} m^3/mol$ (Ref. [35])
$\overline{V}_{Li}$	partial molar volume of Li in the electrode, $8.8 \times 10^{-6} m^3/mol$ (Ref. [35])
$\langle x \rangle$	dimensionless average solid phase lithium concentration (i.e. within the particle) along the porous electrode
x_s	dimensionless surface concentration in the solid particle
δ_n	thickness of the Li-Si composite electrode, m
δ_s	thickness of the separator, m
δ_p	thickness of the lithium foil, m
ϵ	porosity of the electrode (in the separator region, it is the porosity of the separator, 0.39)
ϵ_{bf}	combined volume fraction of the binder and inert filler in the composite electrode
ρ_{sei}	density of species SEI, kg/m^3
ϕ_1	matrix phase electrical potential, V
ϕ_2	solution phase electrical potential, V
η	surface overpotential in the composite electrode, V
α_a, α_c	anodic and cathodic transfer coefficients for the electrochemical reaction at the composite electrode, each taken to be 0.5 in this work
κ_{eff}	effective conductivity of the electrolyte, S/m
κ	conductivity of the electrolyte, S/m
σ_b	bulk conductivity of solid matrix, 33 $[S/m]$ (Ref.[20])
σ_{eff}	effective conductivity of the solid matrix, S/m

both ends of the separator ($x = \delta_n$ and $x = \delta_s$), are electronically insulating. To maintain ionic charge balance in the electrolyte, current collector/electrode boundaries ($x = 0$ and $x = \delta_p$) are insulating for ionic currents.

The mathematical model presented here closely follows the model based on porous electrode theory [18–22]. In the earlier lithium-ion cell models [18,19,32], it is assumed that electrode porosity (ϵ) is constant and that volume changes can be neglected. The solvent can then be chosen as a reference species, setting its velocity to zero and neglecting its flow. Since the void volume changes significantly in Li-Si systems, however, this assumption is no longer valid, and the solvent velocity cannot be treated as zero. For Li-Si type systems, convection plays a role in the transport of the species due to porosity changes. Consequently, a superficial volume average velocity is chosen as the reference ($v^{\#}$). A material balance of the electrolyte ions in the porous electrode is then defined as [20,33]:

$$\frac{\partial (\epsilon c)}{\partial t} = \nabla \cdot \left(\epsilon D_{eff} \nabla c \right) - c_0 \overline{V}_0 \frac{i_2 . \nabla t_+^0}{z_+ \nu_+ F} - \nabla \cdot \left(c \nu^{\#} \right) + c_0 \overline{V}_0 \frac{a j_n \left(1 - t_+^0 \right)}{\nu_+} \tag{1}$$

Here, ϵ is a function of both position and time. Symbols used in the above and the following equations are explained in Table 1.

Since the performance of a lithium-silicon composite electrode at 296 K is modeled in this work, $Li_{15}Si_4$ is taken to be the most lithiated phase. The particle size in the Li-Si system will not remain constant during lithiation/delithiation. For single electrode reactions, the porosity change in the composite electrode is related to volume change and is defined as [20,34]:

$$\frac{\partial \epsilon}{\partial t} = -\frac{a s_+}{F} i_n \left(\tilde{V}_{LiSi4/15} - \tilde{V}_{Si4/15} \right) \tag{2}$$

Here, $\tilde{V}_{LiSi_{4/15}}$ ($0 < x \leq 3.75$) and $\tilde{V}_{Si_{4/15}}$ are the molar volume of $Li_xSi_{4/15}$ and bare silicon in composite electrode, respectively. $\tilde{V}_{LiSi4/15}$ is defined as [20,35]

$$\tilde{V}_{LiSi_{4/15}} = \frac{4}{15} \left(\overline{V}_{Si} + 3.75 \langle x \rangle \overline{V}_{Li} \right) \tag{3}$$

The particle size in the Li-Si system will not remain constant during lithiation/delithiation. Chandrasekaran et al. [25] derived an expression to evaluate the changing particle size (R_{sp}):

$$R_{sp} = R_s \left(1 + \frac{3.75 \overline{V}_{Li} \langle x \rangle}{\overline{V}_{Si}} \right)^{1/3}; \quad \langle x \rangle = c_{s_{avg}} / c_{max} \tag{4}$$

R_{sp} is used to predict specific interfacial area ($a = 3(1 - \epsilon - \epsilon_{bf})/R_{sp}$) which describes interfacial transport in the silicon electrode.

Charge-transfer kinetics at the surface of the particle for lithiation/delithiation in the silicon composite electrode is assumed to be described by the Butler--Volmer equation

$$i = i_0\left[exp\left(\frac{\alpha_a F\eta}{RT}\right) - exp\left(\frac{-\alpha_c F\eta}{RT}\right)\right] \quad (5)$$

The overpotential (η) for Faradaic process is defined as

$$\eta = \phi_1 - \phi_2 - U(x_s) \quad (6)$$

where U is the equilibrium potential of the silicon composite electrode as a function of state of charge (SoC, $x_s = c_s/c_{max}$), and ϕ_1 and ϕ_2 are the potential of the solid phase and the electrolyte phase, respectively.

At the working current collector, the applied current (I_{app}) is related to the transport of electronic charges at the current collector-electrode interface, and thus the boundary condition becomes:

$$\left.\frac{\partial\phi_1}{\partial x}\right|_{x=0} = -\frac{I_{app}}{\sigma_{eff}} \quad \text{at} \quad x = 0 \quad (7)$$

where σ_{eff} is the effective electronic conductivity of the solid matrix and is defined as:

$$\sigma_{eff} = \sigma_b(1 - \epsilon - \epsilon_{bf})^p \quad (8)$$

σ_b is electronic bulk conductivity of solid matrix, ϵ_{bf} is the combined volume fraction of the binder and inert filler in the composite electrode and p is the tortuosity factor.

In porous media, transport properties must be modified to account for the actual path length of the species. Therefore, in the composite electrodes, effective diffusivity (D_{eff}) and effective ionic conductivity in the electrolyte (κ_{eff}) are given by:

$$D_{eff} = D_{Li^+}\epsilon^p \quad (9)$$

and

$$\kappa_{eff} = \kappa\epsilon^p \quad (10)$$

The work presented here closely follows that by Chandrasekaran et al. [20], where more detailed equations and model description can be found. In addition to that, the most prevailing source of capacity fade lithium ion batteries is the loss of lithium ions to the SEI. The rate of SEI formation reaction is affected both by the diffusion rate across the surface film and by the surface kinetics [36]. Following the work of Safari et al.[36], the local current density of the SEI formation reaction (J_S) is calculated by the cathodic Tafel expression below:

$$J_S = i_{0,s}exp\left(-\frac{\alpha_{c,sei}F}{RT}\eta_s\right) \quad (11)$$

where $i_{0,s}$ is the exchange current density and η_s is the overpotential for the SEI formation. The SEI layer growth rate (i.e., its increase in thickness) is then described by [37]:

$$\frac{d\delta}{dt} = -\frac{J_S m_{sei}}{\rho_{sei}F} \quad (12)$$

$$\delta = \frac{t}{\tau}\left(\sqrt{\frac{2m_{sei}C_S D_{sei}\tau}{\rho_{sei}}} - \frac{D_{sei}}{k}\right) \quad (13)$$

where δ is the thickness, ρ_{sei} is the density and m_{sei} is the molar mass of the SEI, respectively. D_{sei} is the diffusivity of the SEI forming species through the SEI, while C_S is the concentration of this species in the bulk of the electrolyte and k is the reaction rate constant. τ is the time spent during one cycle at the voltage of SEI formation. Thus, t/τ is the number of cycles. Thereby, Eqs. (12) and (13) give the rate of formation of SEI as caused by side reactions and the increase in SEI thickness with cycle number, respectively.

3.1. Numerical simulation

The COMSOL Multiphysics 5.4 lithium ion battery module was used to implement the model, and finite element methodology was applied to solve Eqs. (1)–(13) along with the domain ODEs and DAEs module. The porous electrode and additional porous electrode material nodes were used to simulate the composite electrode materials. Porosity change of the composite anode as determined by Eq. (2) were passed from the domain ODE module to simulate the porosity changes in the composite electrode. For the graphite part of the composite anode, the electrode volume fraction was kept fixed while for silicon it varied in accordance with Eqs. (2) and (4). Physics controlled mesh settings were used and the same mesh settings were used for time studies. A default MUMPS solver was used for the time dependent matrix equations.

4. Results and discussion

4.1. Simulation results

Porosity changes in silicon-graphite (1:2.7) composite electrode during galvanostatic charging and discharging are here investigated using a half-cell model. The galvanostatic lithiation was stopped when the cell potential reached 50 mV, while the cut-off voltage for delithiation was set to 1.50 V. Silicon particles were considered being spherical while the graphite particles were considered as flakes. The initial electrode volume fraction for graphite is 0.45 while for silicon it is 0.15; the rest being void pores (0.4). All parameters used in the simulation are listed in Table 2. The initial thickness of the SEI was assumed to be 1 nm after precycling. Simulations were conducted at high initial porosity of the composite anode to provide enough space for expansion of the silicon particles without changing the dimension of electrode. It is considered that there is no significant expansion of the graphite particles, and hence the volume fraction of graphite in the electrode is fixed while the silicon volume fraction changes according to Eq. (2).

Fig. 1 (a) shows the variation of the cell potential of the composite electrode during galvanostatic cell discharge (lithiation of the composite electrode) and charge (delithiation of the composite electrode) at C/2 (23.5 A/m^2) rate. This figure displays the robustness of the model. Most of the electrode is being utilized during the lithiation and delithiation as there are no restrictions being implied on the use of maximum electrode porosity. Fig. 1(b) gives the variation of cell potential with the capacity of the composite electrode at 1C and C/2 rate. It can be seen that at the lower rate (C/2), the electrode is being fully utilized - or the maximum capacity is achieved - before the lower cut-off potential is reached. However, when the rate is higher than C/2, the electrode capacity decreases significantly due to the lower utilization of active material, following from higher losses; i.e. ohmic drop, activation overpotential and mass transport limitations. When the porosity of the electrode decreases with lithiation, the effective electrolyte conductivity also decreases which further increases of the ohmic drop. This leads to a faster drop to the cut-off potential when applying a high rate.

At C/2 rate, the change in electrode porosity for galvanostatic charge and discharge can be seen in Fig. 2. As mentioned above, the initial electrode porosity is 0.4. It can be seen that the electrode reaches a complete lithiation before the porosity is completely utilized. Hysteresis is, however, observed for the lithiation and delithiation curves, and the porosity does not reach the initial value at the end of delithiation. This is directly correlated to the hysteresis in the voltage curve (Fig. 1(a)), which most likely originates in SEI layer formation, polarization and/or an ohmic drop. Using lower rates than C/2 should thereby be an effective way to reach the initial value of the porosity [20].

Table 2
Table of parameters values

| Parameter	Description	Value[Unit]
cl_0	Electrolyte concentration	$1000\ [mol/m^3]$
c_{max}^{G}	Max Li concentration in graphite electrode	$31507\ [mol/m^3]$
c_{max}^{Si}	Max Li concentration in silicon electrode	$278000\ [mol/m^3]$
c_{init}^{G}	Initial Li concentration in graphite electrode	$220\ [mol/m^3]$
c_{init}^{Si}	Initial Li concentration in silicon electrode	$1946\ [mol/m^3]$
D_{Si}	Diffusion coefficient of lithium in silicon particles	$1.2 \times 10^{-16}[m^2/s]$
D_G	Diffusion coefficient of lithium in graphite particles	$1.4 \times 10^{-13}[m^2/s]$
$i_{0,s}$	Exchange current density for parasitic reaction	$1 \times 10^{-10}[A/cm^2]$
k_{Si}	Intercalation and deintercalation reaction rate coefficient for silicon	$3 \times 10^{-9}[m/s]$
k_G	Intercalation and deintercalation reaction rate coefficient for graphite	$2 \times 10^{-11}[m/s]$
k_{Li}	Reaction rate coefficient for silicon	$1 \times 10^{-6}[m/s]$
m_{sei}	Average molecular weight of SEI	$0.16\ [kg/mol]$
p	Tortousity factor	1.5
R_G	Radius of graphite active particles in composite anode	$8[\mu m]$
R_s	Radius of silicon active particles in composite anode	$1.7[\mu m]$
T	Temperature	$296\ [K]$
s_+	s_+ stoichiometric coefficient of + species in electrode reaction	-1
ρ_{sei}	Density of SEI	$1.6 \times 10^3[kg/m^3]$
κ_{sei}	SEI film conductivity	$1 \times 10^{-6}[S/m]$
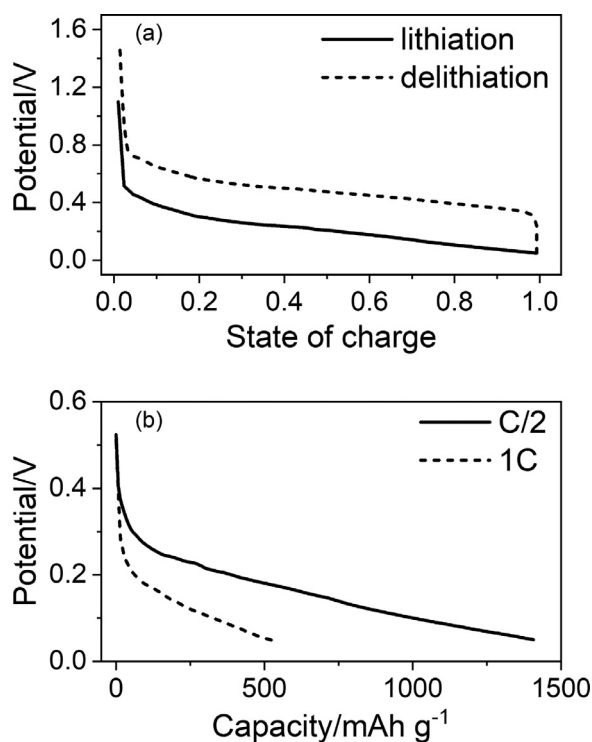
Fig. 1. (a) Simulated charging and discharging profile of a silicon-graphite composite electrode at C/2 rate. (b) Simulated variation of cell potential with the capacity of composite electrode at 1C and C/2 rate.

Fig. 2. Electrode porosity change vs. state of charge of the graphite-silicon composite electrode at C/2 rate.

Fig. 3 shows the change in porosity of the composite electrode across the length of the electrode. At t = 0, the porosity is 0.4, but with lithiation it decreases with time. At early stages, this process is uniform, but as the lithiation proceeds, the porosity changes become non-uniform across the distance in the electrode, with a higher loss of porosity at the electrode-separator interface than at electrode-current collector interface. This occurs due to the better availability of lithium ions towards the electrode-separator interface, while the lithium ion concentration starts to decrease when moving away from this interface and into the bulk of the electrode. As the porosity decreases, the effective electrolyte phase conductivity decreases in the composite electrode, which in turn leads to an increased polarization in the cell. At C/2 rate, the potential
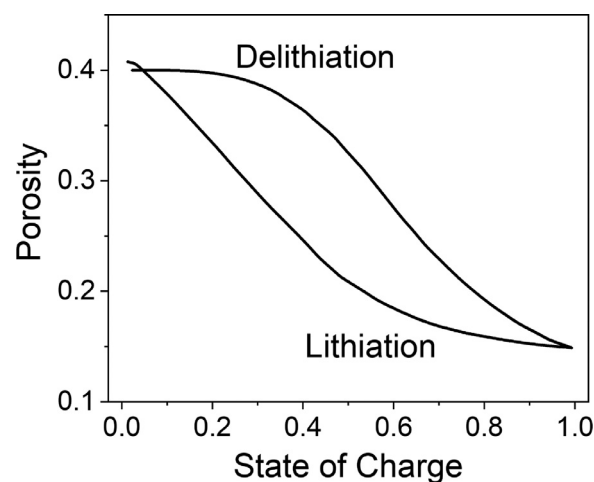
drops to the cut-off value (Fig. 1(b)), before all the available porosity is utilized. Thus, a high initial porosity of silicon or silicon composite electrodes is useful at low rates, but is less advantageous at high rates. This is more clearly seen in the Fig. 3(b), where data for 3C rate is shown. Here, non-uniformities across the electrode length appear also at early stages of lithiation.

Fig. 4 presents the change in radius of the silicon particles (using Eq. (4)) with state of charge of the composite electrode during galvanostatic lithiation at 1C and C/2 rates. The initial radius of the silicon particles is 1.7 μm. For 1C and C/2 rate, the radius increases up to 2.1 and 2.4 μm, respectively, when the cut-off is reached. This corresponds to approximately 23 and 48% increase in the silicon volume fraction, and a corresponding decrease in electrode porosity. The lower decrease in porosity at higher rates is due to that the cut-off is reached at earlier states of lithiation. It should be pointed out that this analysis is done under the assumption that there are no dimensional changes in the electrode.

4.2. Comparison with experiment

In the following section, the model described in this manuscript is compared with the experimental results to show its strength and applicability. The electrochemical characterization is performed using the procedures described in the experimental section. During
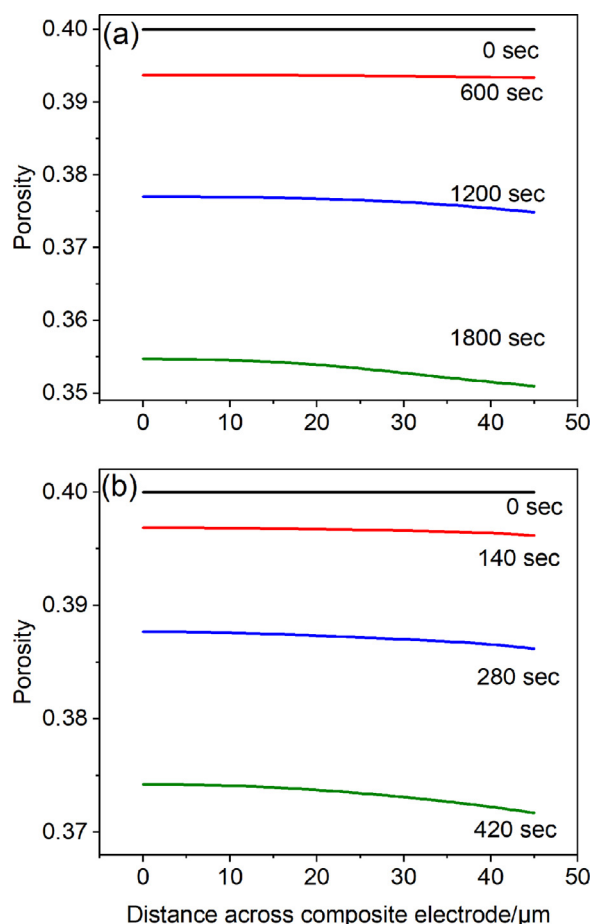
Fig. 3. Variation of composite electrode porosity along the cross-sectional distance across the silicon-graphite composite anode during lithiation (a) at C/2 and (b) 3C rate. The left side of the x-axis represents the electrode-current collector interface while the right side represents the electrode-separator interface in the cell.
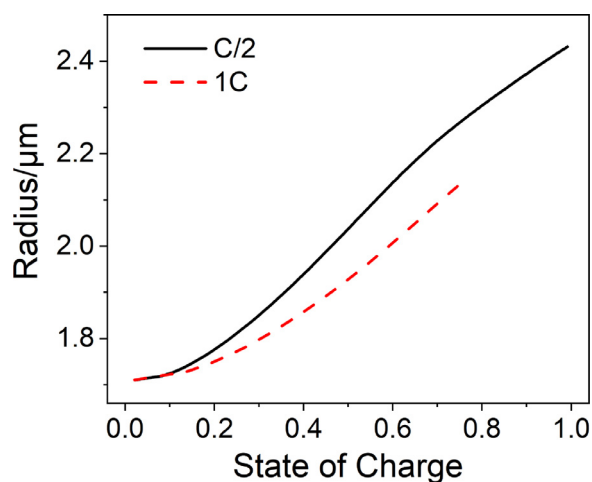

Fig. 4. Variation of the silicon particle radius with state of charge of the electrode during galvanostatic lithiation at C/2 and 1C rates.

cycling at C/2, the lithiation step was limited to a constant lithiation capacity of 800 $mAh\,g^{-1}$, which corresponds to 78.8% SoC. For silicon-based electrodes, capacity limited cycling is preferable to avoid severe damage to the electrode and prolong cycle life. Furthermore, it mimics a full cell lithium ion battery in which the positive electrode is the one determining the cell capacity [11,38]. The silicon-graphite composite electrode displayed stable cycling

for 30 cycles, despite the Coulombic efficiency being only 97% (Fig. 5(a)). Afterwards, the capacity starts to fade continuously together with the Coulombic efficiency until the cell fails after 60 cycles. The lower delithiation capacity compared to lithiation indicates that degradation reactions are occurring in the battery [39]. This behavior is likely due to a loss of lithium inventory which subsequently limits the lithiation reaction [40]. The limited amount of electrolyte used in the cells can also explain the capacity fade, as it is rapidly consumed due to the high mass loading of the electrodes and the lithium metal used in the half cells. To prove this point, additional experiments were carried out with higher amount of electrolyte (80 μL), and the capacity fade was also significantly delayed (Figure S1). These results indicate that the amount of electrolyte affects the battery performance, but that it is not the only contributing factor to the fast capacity fade.

The voltage profiles, in turn, can give additional information regarding the behavior of the battery (Fig. 5(b)). During lithiation, the effect of the increase in overpotential is clear as the onset of the reduction potential decreases with the number of cycles. Thus, the cut-off voltage of 0.05 V is reached earlier and a constant voltage step is needed to achieve the desired capacity. After 30 cycles, the increase in overpotential is even more significant and most of the lithiation occurs during the constant voltage step. In the case of delithiation, there is no significant increase in overpotential until cycle 37. The observed increase in polarization could be due to an increase in cell resistance by electrolyte degradation, continuous SEI growth or electrode cracking.

Furthermore, the rate capability of the system has been investigated at different C-rates. Fig. S2 shows that the voltage profiles are very similar for C/20 and for C/10 without any signs of polarization. The capacity for both C-rates is different due to that the C/20 cycling was not performed with capacity limitation, while at C/10 and higher rates used a limited of 800 $mAh\,g^{-1}$. When further increasing the C-rate to C/2 and 1C, the overpotential increases and the cutoff voltage during lithiation was reached earlier. This indicates a rise in cell resistance and limited electrochemical reactivity of the electrode. Increasing the current also leads to slightly lower Coulombic efficiency as the delithiation capacity is lower than during lithiation, again indicating that more degradation reactions occur at higher currents [39].

For a straight-forward comparison of the experimental and simulation cycling results, an initial volume fraction of 0.154 silicon, 0.42 graphite and 0.126 binder are used in simulation. This equals the volume fractions of the composite electrode components used in the experiments. The initial porosity of the composite electrode is 0.3, which is still high considering the used current rate in the experiment and the capacity cut-off limit (78.8% SoC), as the entire electrode material does not need to be utilized (to reach full SoC). The simulated cycling is done at the same experimental conditions as mentioned above. Fig. 6 shows a comparison between the experimental and simulated voltage profiles of these cells as function of time. Accelerated ageing is used in these simulation results[41], and is implemented as a side-reaction causing SEI layer formation and dissolution (Eq. 12). More details about accelerated aging are given in the supporting information. Thus, the second cycle of the simulation results is equivalent to the 25th cycle of the experiment, and employed to reduce the simulation time. Other parameters used in this section are listed in Table 2.

The voltage curves display an interesting behavior during lithiation after the 3rd cycle in Fig. 5(b). Where early cycles show an extended plateau at ca. 0.2 V, a more rapid drop of voltage towards < 0.1 V is seen for the 30th cycle, and even more pronounced for the 50th cycle. In the simulations, this dramatic drop of potential cannot be captured by SEI layer formation alone: the SEI grows from 1 to 50 nm between these cycles, corresponding to an increase in SEI layer resistance of only $5 \times 10^{-2}\ \Omega\,m^2$. One hypoth-
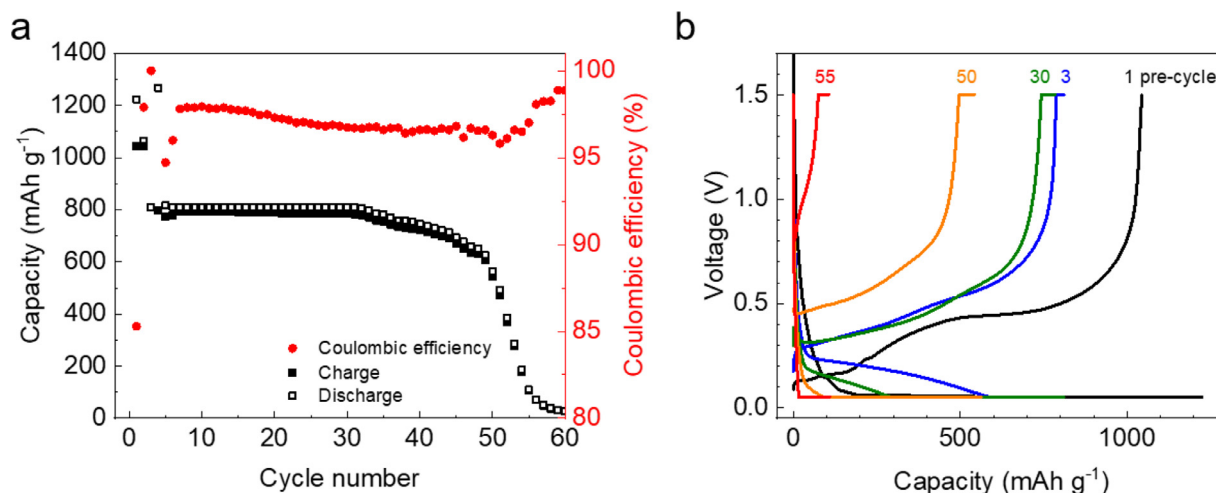
Fig. 5. Electrochemical characterization of silicon-graphite half-cells: (a) long-term cycling performance and (b) voltage profiles of selected cycles.
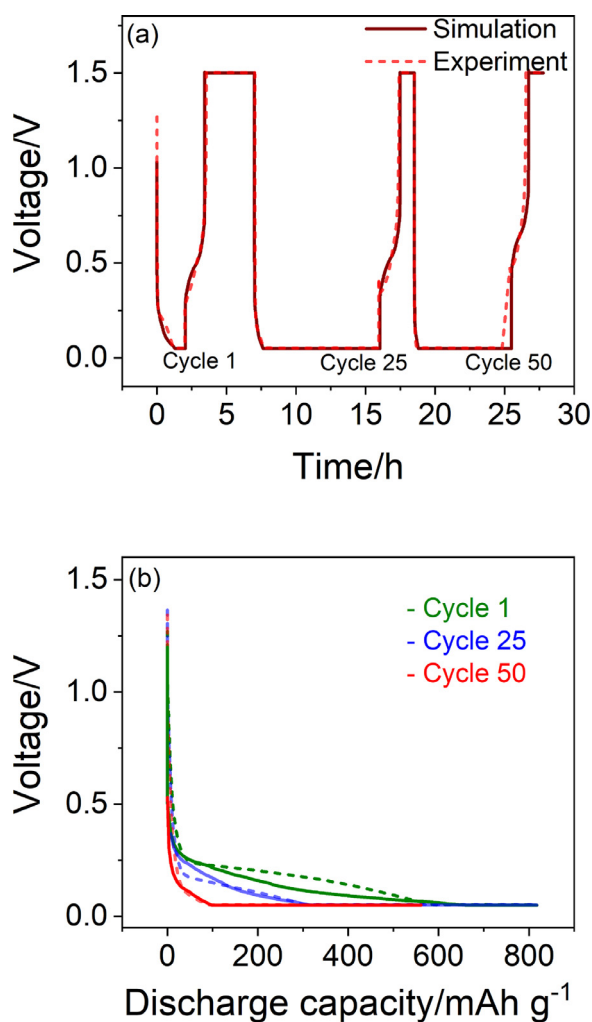

Fig. 6. (a) Comparison of simulated and experimental voltage profile vs. time in silicon-graphite composite half-cell. The time scales of the experimental data are shifted to show these three cycles consecutively. (b) voltage profile vs. discharge capacity for cycle 1, 25 and 50 of a silicon-graphite composite half-cell. The dashed curves represent experimental data while solid curves represent simulated results.

esis is therefore that this potential drop is instead related to a decrease in the solid phase diffusivity of lithium ions in the active material of the composite anode, as also reported earlier for nano-Si composite electrodes [38]. It is a well-known fact that silicon or silicon-based electrodes with particle sizes in micron range might show cracks/fracture upon electrochemical cycling [11,35], which can influence the solid phase transport. In this context, it has also been shown that with carefully designed electrode formulations, good cycling stability (e.g., 200 cycles at a limited electrode capacity of 800 $mAh\,g^{-1}$ [42]), has been demonstrated with composite electrodes using similar compositions and materials; i.e., this capacity degradation can be avoided.

The changes in solid matrix diffusivity due to that the formation of electrode microcracks increases tortuosity in the diffusion pathways of Li^+ have previously been modelled by Barai et al. [43]. They also formulated an expression for the effective diffusivity and its correlation to the microcrack density [44], which in this work has been adopted for Si-based electrodes: $D_{eff}^{Si} = D_{Si}(1 - f_{bb})^{\gamma}$ where D_{Si} denotes the solid phase diffusivity of lithium ions in the silicon active materials when no mechanical degradation occurs. f_{bb} is the microcrack density while γ is an exponent that is estimated from the concentration gradient of Li^+. Due to lack of experimentally determined values for f_{bb} and γ, D_{Si} is used as fitting parameter when comparing the simulation results to the experimental counterparts; the value used here being $6 \times 10^{-17} m^2/s$.

Fig. 6 displays a comparison of experimental and simulated voltage-discharge capacity curves, where the added effect of microcracks is included into the applied model (comparison of more experimental and simulated voltage-discharge capacity curves are shown in Figure S3). It can then be observed that the proposed model here for the silicon-graphite composite anode captures the experimental data satisfactorily. Comparison of experimental and simulated voltage-charge capacity curves are shown in Figure S4. The simulated cycling data shows an abrupt voltage rise after 0.7-0.8 V, which is due to that the delithiation reaction reaches completeness. A similar, but not as abrupt rise is seen in the corresponding experimental data. Hence, it can be stated that the capacity fading observed in the silicon-graphite composite anode is indeed caused by a decrease in the solid phase diffusion coefficient due to increase in tortuosity, which contributes more significantly to the capacity fading than the SEI layer growth. Figure S5 stresses the importance of including effect of microcraks into the applied model.

Moreover, this highlights that for a silicon-graphite composite electrode, a careful design of composition, i.e. relative fractions,

type of graphite and silicon, porosity and binder system are crucial for the electrochemical performance. In the results presented here, the high degree of lithiation of the electrodes leads to a more rapid electrode failure when compared to electrodes studied previously with similar material but with higher silicon content, but where a lower utilization of the silicon has been applied [42]. In fact, when subject to pre-lithiation [45], 245 cycles were demonstrated for a full cell with a $LiNi_{0.8}Co_{0.15}Al_{0.05}O_2$ cathode and a Si-graphite composite anode of 60 wt% of similar silicon, which shows that Si-based composites can display more appealing cycling data. It thus appears that the high lithiation and corresponding loss of porosity, probably in combination with a flaky graphite, makes the active material more susceptible to cracking, since this explanation correlates well with the modelling results.

5. Conclusions

In this work, a one-dimensional model for silicon-graphite composite electrodes has been developed, which includes volume expansion/contraction of the silicon particles during lithiation/delithiation, and has been implemented in lithium half-cells. SEI layer formation and growth are also included in the model. Comparison with experimental time data indicates that the model well captures the relationship between porosity changes and capacity fading when the effects of microcracks are included in the simulations. The results clearly show that the capacity fading observed in the silicon-graphite composite anode is caused by a decrease in the solid phase diffusion coefficient of silicon particles, which contributes more to the capacity fading than the SEI layer growth. Thereby, this model can be used to investigate how these composite graphite-silicon electrodes can be made more efficient by varying the ratio of graphite and silicon.

Declaration of Competing Interest

The authors declare that they have no known competing financial interests or personal relationships that could have appeared to influence the work reported in this paper.

Credit authorship contribution statement

Shweta Dhillon: Writing - original draft, Software, Methodology. **Guiomar Hernández:** Validation, Writing - review & editing. **Nils P. Wagner:** Resources, Writing - review & editing. **Ann Mari Svensson:** Funding acquisition, Conceptualization, Writing - review & editing. **Daniel Brandell:** Funding acquisition, Supervision, Writing - review & editing.

Acknowledgments

References

[1] M.N. Obrovac, L. Christensen, Structural Changes in Silicon Anodes during Lithium Insertion/Extraction, Electrochem. Solid-State Lett. 7 (5) (2004) A93–A96, doi:10.1149/1.1652421.

[2] V.L. Chevrier, L. Liu, D.B. Le, J. Lund, B. Molla, K. Reimer, L.J. Krause, L.D. Jensen, E. Figgemeier, K.W. Eberman, Evaluating Si-based materials for Li-ion batteries in commercially relevant negative electrodes, Journal of the Electrochemical Society 161 (5) (2014) 783–791, doi:10.1149/2.066405jes.

[3] D. Ma, Z. Cao, A. Hu, Si-based anode materials for li-ion batteries: A mini review, Nano-Micro Letters 6 (4) (2014) 347–358, doi:10.1007/s40820-014-0008-2.

[4] M. Wetjen, D. Pritzl, R. Jung, S. Solchenbach, R. Ghadimi, H.A. Gasteiger, Differentiating the degradation phenomena in silicon-graphite electrodes for lithium-ion batteries, Journal of the Electrochemical Society 164 (12) (2017) A2840–A2852, doi:10.1149/2.1921712jes.

[5] R. Petibon, V.L. Chevrier, C.P. Aiken, D.S. Hall, S.R. Hyatt, R. Shunmugasundaram, J.R. Dahna, Studies of the Capacity Fade Mechanisms of LiCoO2/Si-Alloy: Graphite Cells, J. Electrochem. Soc. 163 (7) (2016) A1146–A1156, doi:10.1149/2.0191607jes.

[6] Z. Chen, L. Christensen, J.R. Dahn, Large-volume-change electrodes for Li-ion batteries of amorphous alloy particles held by elastomeric tethers, Electrochemistry Communications 5 (11) (2003) 919–923, doi:10.1016/j.elecom.2003.08.017.

[7] H. Zhang, P.V. Braun, Three-dimensional metal scaffold supported bicontinuous silicon battery anodes, Nano Letters 12 (6) (2012) 2778–2783, doi:10.1021/nl204551m.

[8] M.T. McDowell, S.W. Lee, J.T. Harris, B.A. Korgel, C. Wang, W.D. Nix, Y. Cui, In situ tem of two-phase lithiation of amorphous silicon nanospheres, Nano Letters 13 (2) (2013) 758–764, doi:10.1021/nl3044508.

[9] C.K. Chan, R.A. Huggins, C.K. Chan, H. Peng, G.A.O. Liu, K. Mcilwrath, X.F. Zhang, R.A. Huggins, Y.I. Cui, High-Performance Lithium Battery Anodes Using Silicon Nanowires High-performance lithium battery anodes using silicon nanowires, Nature Nanotechnology 3 (January) (2008) 31–35, doi:10.1038/nnano.2007.411.

[10] H. Wu, G. Chan, J.W. Choi, I. Ryu, Y. Yao, M.T. Mcdowell, S.W. Lee, A. Jackson, Y. Yang, L. Hu, Y. Cui, Stable cycling of double-walled silicon nanotube battery anodes through solid-electrolyte interphase control, Nature Nanotechnology 7 (5) (2012) 310–315, doi:10.1038/nnano.2012.35.

[11] M.N. Obrovac, V.L. Chevrier, Alloy negative electrodes for Li-ion batteries, Chemical Reviews 114 (23) (2014) 11444–11502, doi:10.1021/cr500207g.

[12] G. Bucci, S.P.V. Nadimpalli, V.A. Sethuraman, A.F. Bower, P.R. Guduru, Measurement and modeling of the mechanical and electrochemical response of amorphous Si thin film electrodes during cyclic lithiation, Journal of the Mechanics and Physics of Solids 62 (1) (2014) 276–294, doi:10.1016/j.jmps.2013.10.005.

[13] E.M. Pell, Diffusion rate of li in si at low temperatures, Phys. Rev. 119 (1960) 1222–1225, doi:10.1103/PhysRev.119.1222.

[14] J.H. Ryu, J.W. Kim, Y.E. Sung, S.M. Oh, Failure modes of silicon powder negative electrode in lithium secondary batteries, Electrochemical and Solid-State Letters 7 (10) (2004) A306–A309, doi:10.1149/1.1792242.

[15] M. Ratynski, B. Hamankiewicz, D.A. Buchberger, M. Boczar, M. Krajewski, A. Czerwinski, A New Technique for In Situ Determination of the Active Surface Area Changes of Li-Ion Battery Electrodes, Batteries & Supercaps 3 (10) (2020) 1028–1039, doi:10.1002/batt.202000088.

[16] M. Ratynski, B. Hamankiewicz, M. Krajewski, M. Boczar, D.A. Buchberger, A. Czerwinski, Electrochemical Impedance Spectroscopy Characterization of Silicon-Based Electrodes for Li-Ion Batteries, Electrocatalysis 11 (2) (2020) 160–169, doi:10.1007/s12678-019-00573-y.

[17] A.A. Franco, A. Rucci, D. Brandell, C. Frayret, M. Gaberscek, P. Jankowski, P. Johansson, Boosting Rechargeable Batteries R&D by Multiscale Modeling: Myth or Reality? Chemical Reviews 119 (7) (2019) 4569–4627, doi:10.1021/acs.chemrev.8b00239.

[18] J.S. Newman, C.W. Tobias, Theoretical Analysis of Current Distribution in Porous Electrodes, J. Electrochem. Soc. 109 (12) (1962) 1183–1191, doi:10.1149/1.2425269.

[19] J. Newman, K.E. Thomas, H. Hafezi, D.R. Wheeler, Modeling of Lithium-ion Batteries, J. Power Sources 119-121 (2003) 838–843, doi:10.1016/S0378-7753(03)00282-9.

[20] R. Chandrasekaran, T.F. Fuller, Analysis of the lithium-ion insertion silicon composite electrode/separator/lithium foil cell, J. Electrochem. Soc. 158 (8) (2011) A859–A871, doi:10.1149/1.3589301.

[21] G. Sikha, B.N. Popov, R.E. White, Effect of porosity on the capacity fade of a lithium-ion battery theory, Journal of the Electrochemical Society 151 (7) (2004) A1104–A1114, doi:10.1149/1.1759972.

[22] S. Srivastav, C. Xu, K. Edström, T. Gustafsson, D. Brandell, Modelling the morphological background to capacity fade in Si-based lithium-ion batteries, Electrochimica Acta 258 (2017) 755–763, doi:10.1016/j.electacta.2017.11.124.

[23] D. Bernardi, E.M. Pawlikowski, J. Newman, Mathematical modeling of LiAl/LiCl,KCl/FeS cells, 1988, 10.1149/1.2095464

[24] R. Pollard, J. Newman, Mathematical Modeling of the Lithium-Aluminum, Iron Sulfide Battery I. Galvanostatic Discharge Behavior, 1981,. 10.1149/1.2127445

[25] R. Chandrasekaran, A. Magasinski, G. Yushin, T.F. Fuller, Analysis of lithium insertion/deinsertion in a silicon electrode particle at room temperature, Journal of the Electrochemical Society 157 (10) (2010) A1139–A1151, doi:10.1149/1.3474225.

[26] J. Yang, B.F. Wang, K. Wang, Y. Liu, J.Y. Xie, Z.S. Wen, Si/C composites for high capacity lithium storage materials, Electrochemical and Solid-State Letters 6 (8) (2003) A154–A156, doi:10.1149/1.1585251.

[27] B. Fuchsbichler, C. Stangl, H. Kren, F. Uhlig, S. Koller, High capacity graphite-silicon composite anode material for lithium-ion batteries, Journal of Power Sources 196 (5) (2011) 2889–2892, doi:10.1016/j.jpowsour.2010.10.081.

[28] C.H. Yim, F.M. Courtel, Y. Abu-Lebdeh, A high capacity silicon-graphite composite as anode for lithium-ion batteries using low content amorphous silicon and compatible binders, Journal of Materials Chemistry A 1 (28) (2013) 8234–8243, doi:10.1039/c3ta10883j.

[29] M. Ko, S. Chae, J. Cho, Challenges in Accommodating Volume Change of Si Anodes for Li-Ion Batteries, ChemElectroChem 2 (11) (2015) 1645–1651, doi:10.1002/celc.201500254.

[30] S.D. Beattie, D. Larcher, M. Morcrette, B. Simon, J.M. Tarascon, Si electrodes for Li-ion batteries-A new way to look at an old problem, Journal of the Electrochemical Society 155 (2) (2008) 158–163, doi:10.1149/1.2817828.

[31] L. Niedzicki, G.Z. Zukowska, M. Bukowska, P. Szczeciński, S. Grugeon, S. Laruelle, M. Armand, S. Panero, B. Scrosati, M. Marcinek, W. Wieczorek, New type of imidazole based salts designed specifically for lithium ion batteries, Electrochimica Acta 55 (4) (2010) 1450–1454, doi:10.1016/j.electacta.2009.05.008.

[32] T.F. Fuller, M. Doyle, J. Newman, ELECTROCHEMICAL SCIENCE AND TECHNOLOGY Simulation and Optimization of the Dual Lithium Ion Insertion Cell, J. Electrochem. Soc 141 (1) (1994) 1–10, doi:10.1149/1.2054684.

[33] J. Newman, K.E. Thomas-Alyea, Electrochemical Systems, 3, John Wiley & Sons, Berkeley, 2012.

[34] J. Newman, W. Tiedemann, Porous-electrode theory with battery applications, AIChE J. 21 (1) (1975) 25–41, doi:10.1002/aic.690210103.

[35] M.N. Obrovac, L. Christensen, D.B. Le, J.R. Dahn, Alloy design for lithium-ion battery anodes, Journal of the Electrochemical Society 154 (9) (2007) A849–A855, doi:10.1149/1.2752985.

[36] M. Safari, M. Morcrette, A. Teyssot, C. Delacourt, Multimodal Physics-Based Aging Model for Life Prediction of Li-Ion Batteries, Journal of the Electrochemical Society 156 (3) (2009) A145–A153, doi:10.1149/1.3043429.

[37] M.B. Pinson, M.Z. Bazant, Theory of SEI formation in rechargeable batteries: Capacity fade, accelerated aging and lifetime prediction, Journal of the Electrochemical Society 160 (2) (2013) A243–A250, doi:10.1149/2.044302jes.

[38] F. Lindgren, D. Rehnlund, R. Pan, J. Pettersson, R. Younesi, C. Xu, T. Gustafsson, K. Edström, L. Nyholm, On the Capacity Losses Seen for Optimized NanoSi Composite Electrodes in Li-Metal Half-Cells, Advanced Energy Materials 9 (33) (2019) 1901608, doi:10.1002/aenm.201901608.

[39] Y. Oumellal, N. Delpuech, D. Mazouzi, N. Dupré, J. Gaubicher, P. Moreau, P. Soudan, B. Lestriez, D. Guyomard, The failure mechanism of nano-sized Si-based negative electrodes for lithium ion batteries, Journal of Materials Chemistry 21 (17) (2011) 6201–6208, doi:10.1039/c1jm10213c.

[40] W.M. Dose, M.J. Piernas-Muñoz, V.A. Maroni, S.E. Trask, I. Bloom, C.S. Johnson, Capacity fade in high energy silicon-graphite electrodes for lithium-ion batteries, Chemical Communications 54 (29) (2018) 3586–3589, doi:10.1039/c8cc00456k.

[41] COMSOL Multiphysics, 1D lithium-ion battery model for the capacity fade tutorial (Version application ID: 12667): COMSOL MultiPhysics, https://www.comsol.se/model/1d-lithium-ion-battery-model-for-the-capacity-fade-tutorial-12667 (2020).

[42] H.F. Andersen, C.E.L. Foss, J. Voje, R. Tronstad, T. Mokkelbost, P.E. Vullum, A. Ulvestad, M. Kirkengen, J.P. Mæhlen, Silicon-Carbon composite anodes from industrial battery grade silicon, Scientific Reports 9 (14814) (2019) 1–9, doi:10.1038/s41598-019-51324-4.

[43] P. Barai, P.P. Mukherjee, Stochastic Analysis of Diffusion Induced Damage in Lithium-Ion Battery Electrodes, Journal of The Electrochemical Society 160 (6) (2013) A955–A967, doi:10.1149/2.132306jes.

[44] P. Barai, K. Smith, C.-F. Chen, G.-H. Kim, P.P. Mukherjee, Reduced Order Modeling of Mechanical Degradation Induced Performance Decay in Lithium-Ion Battery Porous Electrodes, Journal of The Electrochemical Society 162 (9) (2015) A1751–A1771, doi:10.1149/2.0241509jes.

[45] N. P.Wagner, K. Asheim, F. Vullum-Bruer, A.M. Svensson, Silicon-Carbon composite anodes from industrial battery grade silicon, Journal of Power Sources 437 (2019), doi:10.1016/j.jpowsour.2019.226884. 226884–10